Chapter 11
MBE Growth of Thin Hexagonal Films Bi_2Te_3, Bi_2Se_3, and Their Alloys on Cubic GaAs (001) Substrates

Xinyu Liu, Y.P. Chen, D.J. Smith, Y.-H. Zhang, C. Liu, M.Z. Hasan, M. Dobrowolska, J.K. Furdyna, J. Fan, H. Cao, T.-L. Wu, and R.E. Pimpinella

Abstract Films of pseudo-hexagonal Bi_2Te_3, Bi_2Se_3, and their alloys were successfully grown by molecular beam epitaxy (MBE) on GaAs (001) substrates. The growth mechanism and structural properties of these films were investigated by reflection high-energy electron diffraction (RHEED), atomic force microscopy (AFM), X-ray diffraction (XRD), high-resolution transmission electron microscopy (HRTEM), and Raman spectroscopy and mapping. The results indicate that the epitaxial films are highly uniform and of high crystalline quality. The electronic band structure of these films was studied by angle-resolved photoemission spectroscopy (ARPES). The results confirm that these films are topological insulators, with a single Dirac cone for the topological surface states. Electric transport measurements were performed on the films, and weak anti-localization (WAL)

X. Liu (✉) • M. Dobrowolska • J.K. Furdyna • R.E. Pimpinella
Department of Physics, University of Notre Dame, Notre Dame, IN 46556, USA
e-mail: xliu2@nd.edu; mdobrowo@nd.edu; furdyna@nd.edu; rpimpine@nd.edu

Y.P. Chen • H. Cao • T.-L. Wu
Department of Physics, Purdue University, West Lafayette, IN 47907, USA
e-mail: yongchen@purdue.edu; cao2@purdue.edu; wu386@purdue.edu

D.J. Smith • J. Fan
Department of Physics, Arizona State University, Tempe, AZ 85287, USA
e-mail: david.smith@asu.edu; jin.fan@asu.edu

Y.-H. Zhang
Center for Photonics Innovation, Arizona State University, Tempe, AZ 85287, USA

School of Electrical, Computer and Energy Engineering, ASU, Tempe, AZ 85287, USA
e-mail: yhzhang@asu.edu

C. Liu • M.Z. Hasan
Department of Physics, Princeton University, Princeton, NJ 08544, USA
e-mail: cliu82@princeton.edu; mzhasan@princeton.edu

H. Li and Z.M. Wang (eds.), *Bismuth-Containing Compounds*, Springer Series in Materials Science 186, DOI 10.1007/978-1-4614-8121-8_11,
© Springer Science+Business Media New York 2013

was observed in the magnetoresistance. Tuning of conductance by gating was demonstrated in top-gated field effect transistor (FET) devices fabricated from these films.

11.1 Introduction

In terms of conventional band theory, solids can be classified either as metals or as insulators. Traditional insulators include covalent insulators and atomic insulators, distinguished by the size of their band gaps, around 1.0 and 10 eV, respectively. Recently, a new type of quantum matter, the topological insulator (TI), has been brought to the attention of the science community, primarily by the ground-breaking theoretical work of Kane and Mele [1, 2]. Following this revolutionary theoretical milestone, quantum spin Hall effect (QSHE) was predicted and observed in two-dimensional (2D) HgTe quantum wells [3, 4], which possess a pair of crossing perfectly conducting edge states and exhibit a quantized resistance of $R = h/2e^2$ [5]. These advances have stimulated intensive search for three-dimensional (3D) TIs, a new state of matter with topologically nontrivial band structure originating from strong spin-orbit coupling [6, 7].

The 3D TIs possess fully gapped bulk states and gapless surface states, which can be described by the Rashba spin-orbit Hamiltonian [1, 8, 9]. These surface states are chiral, i.e., they possess a well-defined spin texture (referred to as spin-momentum locking), and they have an energy-momentum spectrum akin to the Dirac cone [10, 11]. Chiral Rashba surface states have a nontrivial band topology protected by time-reversal symmetry, and are thus robust against coherent backscattering and smooth perturbations invariant under time reversal [9]. Unlike 2D TIs, 3D TIs at present are experimentally established largely by surface-sensitive probes, such as scanning tunneling microscopy (STM) and angle-resolved photoemission spectroscopy (ARPES). These measurements have confirmed 3D topological insulating behavior in a number of materials—$Bi_{1-x}Sb_x$ [12], Bi_2Se_3 [13, 14], Bi_2Te_3 [15, 16], and Sb_2Te_3 [17]—all of which show an insulating energy gap in the bulk and gapless surface state(s) with a Dirac-like linear band dispersion. Further experimental studies of these systems have provided evidence of the existence of chiral surface states, and confirmed their protection by time-reversal symmetry [9]. For example, spin-resolved ARPES was used to measure spin polarization of the surface states, demonstrating the correlation between spin and momentum in these TI materials [17]. Moreover, a combination of STM and spin-resolved ARPES demonstrated that scattering between states with opposite momenta is strongly suppressed in the presence of time-reversal-invariant disorder in these materials [18]. The discovery of TIs has thus revolutionized our understanding of insulating behavior, and has stimulated intense investigation on the interaction between TIs and other forms of quantum matter. One should note that the rich new physics which occurs in TI-based structures, in addition to its fundamental interest, could also contribute to the development of a platform for many novel applications.

In order to study fundamental TI properties, high quality TI films need to be interfaced with superconductors, ferromagnets, or other complex materials [5, 9]. In this context, molecular beam epitaxy (MBE) is especially attractive, because of its capability for growing multilayer heterostructures under highly controlled conditions, so that defect formation is minimized during growth. Most efforts to fabricate TI films by MBE have so far been carried out using substrates with either hexagonal or threefold symmetric surface structures, such as Si (111) [19, 20], graphene [21], sapphire (0001) [21], $SrTiO_3$ (111) [22], and GaAs (111) [23]. Because representative spintronic materials, such as (Ga,Mn)As, are most commonly grown on GaAs (001) substrates [24], and Fe films of very high crystalline perfection can also be grown on GaAs (001) or (110) substrates [25], we are actively pursuing MBE growth of Bi_2Te_3, Bi_2Se_3, and their alloys on GaAs (001) substrates [26, 27], with the goal of combining these electronic materials into multifunctional device configurations in the future.

In this chapter, we describe MBE growth of hexagonal Bi_2Te_3, Bi_2Se_3, and their alloys on such symmetrically mismatched GaAs (001) substrates. This novel growth mode may enable one to combine almost any pair of layered materials together, thus allowing us to produce a variety of high quality hybrid heterostructures. Our work reveals the unique layer-by-layer growth of these materials in a pseudo-hexagonal layered structure—a crystalline form that involves sequences of five atomic layers [quintuple layers (QLs), e.g., Te-Bi-Te-Bi-Te or Se-Bi-Se-Bi-Se], each atomic Te/Se or Bi layer within the QL forming a 2D hexagonal lattice perpendicular to the growth axis (the *c*-axis). Our results thus suggest a powerful new possibility for combining the highly attractive properties of TI materials with traditional electronic materials that are compatible with the cubic structure, for the purpose of constructing new multifunctional device configurations.

11.2 MBE Growth of Bi_2Se_3 and Bi_2Te_3 Films

The TI films, including Bi_2Te_3, Bi_2Se_3, and their ternary alloys, were grown using a dual chamber Riber 32 solid-source MBE system. The Bi, Te_2, and Se_2 fluxes were generated by standard effusion cells installed in a modified II–VI MBE chamber. The structure and thickness of the films were monitored in situ by reflection high-energy electron diffraction (RHEED). The growth sequence was as follows. First, an epi-ready GaAs (001) substrate was heated to 600 °C for deoxidation in the III–V MBE chamber. This was followed by deposition of a 100-nm GaAs buffer layer. This modified substrate was then transferred to the II–VI MBE chamber through an ultrahigh vacuum connection. The growth of the TI film was initiated by deposition of a series of monolayers of Te-Bi-Te-Bi-Te or Se-Bi-Se-Bi-Se—a quintuple layer (QL)—in atomic layer epitaxy (ALE) fashion at room temperature. During this process, the (2×4) RHEED pattern of GaAs buffer (as shown in Fig. 11.1a, b) disappeared, indicating that an amorphous film had been deposited.

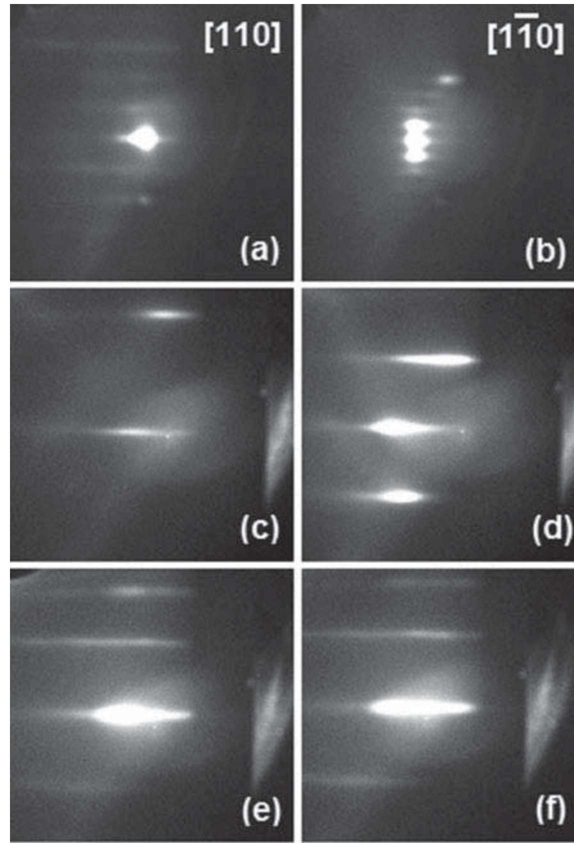

Fig. 11.1 RHEED patterns observed for two specific orientations of GaAs (001) substrate during MBE growth of Bi_2Te_3 and Bi_2Se_3. (**a**) and (**b**) correspond to GaAs (001) surface; (**c**) and (**d**) show single-phase growth mode (Bi_2Te_3); (**e**) and (**f**) indicate dual-phase growth mode (Bi_2Se_3). After ref. [30]

The substrate was then gradually heated to 300 °C, and a streaky unreconstructed RHEED pattern appeared (see Fig. 11.1c–f). The MBE growth of Bi_2Te_3, Bi_2Se_3, or their alloys was subsequently performed under Te_2- or Se_2-rich conditions with $T_{substrate}=300$ °C. The RHEED patterns shown in Fig. 11.1c–f were maintained throughout the entire growth process. It is important to note that the observed RHEED pattern showed six recurrences during each rotation of the substrate, which confirmed the *c*-axis growth of the TI films, with the *a*-axis lying along either the [110] or the $[1\bar{1}0]$ direction of the GaAs (001) substrate. Two types of RHEED patterns were observed at this stage, depending on the annealing process. As shown in Fig. 11.1c, d typically observed in the case of Bi_2Te_3 (QLs of Bi_2Te_3 usually survive for a longer annealing time than for Bi_2Se_3), the annealing yielded an unreconstructed pattern with distinct features observed for GaAs [110] and $[1\bar{1}0]$ directions, respectively. We attribute this to the hexagonal surface symmetry of the TI layer. Alternately, in the case of MBE growth of Bi_2Se_3, we typically observed the same RHEED patterns for both GaAs [110] and $[1\bar{1}0]$ directions, as shown in Fig. 11.1e, f. Note that the RHEED pattern in Fig. 11.1e, f is actually a combination

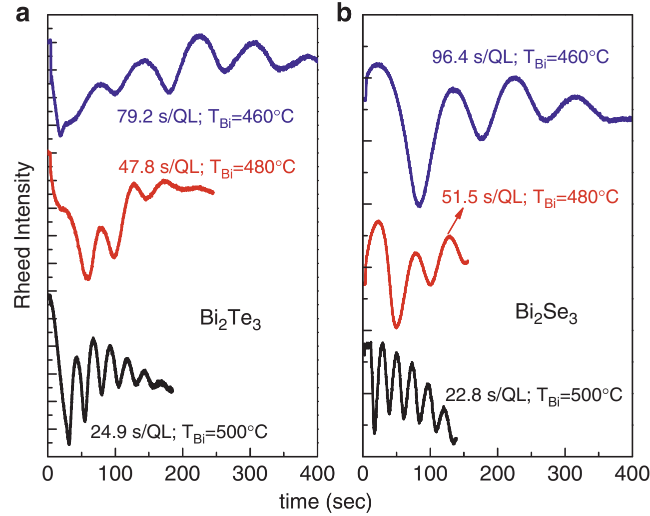

Fig. 11.2 RHEED intensity oscillations of the specular point versus growth time for different Bi cell temperatures T_{Bi}: (**a**) Bi_2Te_3; (**b**) Bi_2Se_3. After ref. [31]

of two distinct patterns, that for the [110] and the $[1\bar{1}0]$ directions in the Fig. 11.1c, d, respectively. We attribute this to the coexistence of two types of hexagonal surfaces perpendicular to each other.

The MBE growth of Bi_2Te_3 and Bi_2Se_3 was then performed under the condition of T_{Te} (or T_{Se}) < $T_{substrate}$ (300 °C) < T_{Bi} (500 °C) with a Se_2(or Te_2):Bi beam equivalent pressure (BEP) ratio ranging from 10:1 to 100:1. At the beginning of the growth clear RHEED oscillations of the specular spot were observed, each oscillation corresponding to the growth of one QL. Figure 11.2 shows RHEED oscillations observed with different temperatures of the Bi cell, T_{Bi}. As the Bi cell temperature was increased, the period of the oscillations decreased, indicating that the growth rate was directly controlled by the Bi flux, and that the growth of the TI films progressed in a QL-by-QL mode.

The same kind of growth is also observed on Ga-rich GaAs (001) surfaces, i.e., surfaces with a (4 × 6) RHEED pattern. We therefore attribute the successful growth of pseudo-hexagonal Bi_2Te_3 and Bi_2Se_3 on GaAs (001) substrates to the weak Van der Waals coupling between the substrate and the TI films, leading to immediate strain relaxation as the interface is forming. Note that the symmetry-mismatched interface between cubic (001) GaAs and pseudo-hexagonal (0001) Bi_2Te_3 or Bi_2Se_3 leads to the appearance of two hexagonal phases with the orientation relationships as either $(110) \parallel (0\bar{1}10)$ or (110) ‖ (1000), indicating an interface effect on the nucleation of the hexagonal phases.

Earlier studies of MBE growth of Bi_2Te_3 on cubic Si (001) substrates [22] appeared to suggest that a hexagonal structure of the substrate surface was essential

for epitaxial growth of Bi_2Te_3 film to succeed. In contrast, our work shows that high quality Bi_2Te_3, Bi_2Se_3, and their alloys can form on GaAs (001) substrates with well-defined crystal orientations. This result suggests that the problems encountered in the MBE growth of Bi_2Te_3 films on Si (001) substrates could be caused by the reactivity of Te with Si [28], rather than being a result of mismatched symmetries at the substrate–TI interface. Our discovery shows that a self-correction process during growth of these layered honeycomb materials may play an important role in overcoming differences between crystal arrangements at interfaces during epitaxy.

11.3 Surface Morphology

Subsequent to MBE growth, the surface morphology of the TI samples was characterized ex situ by atomic force microscopy (AFM). Figure 11.3 shows AFM images of Bi_2Te_3 and Bi_2Se_3 films deposited at a growth rate of 2 nm/min, at the Te_2/Bi BEP

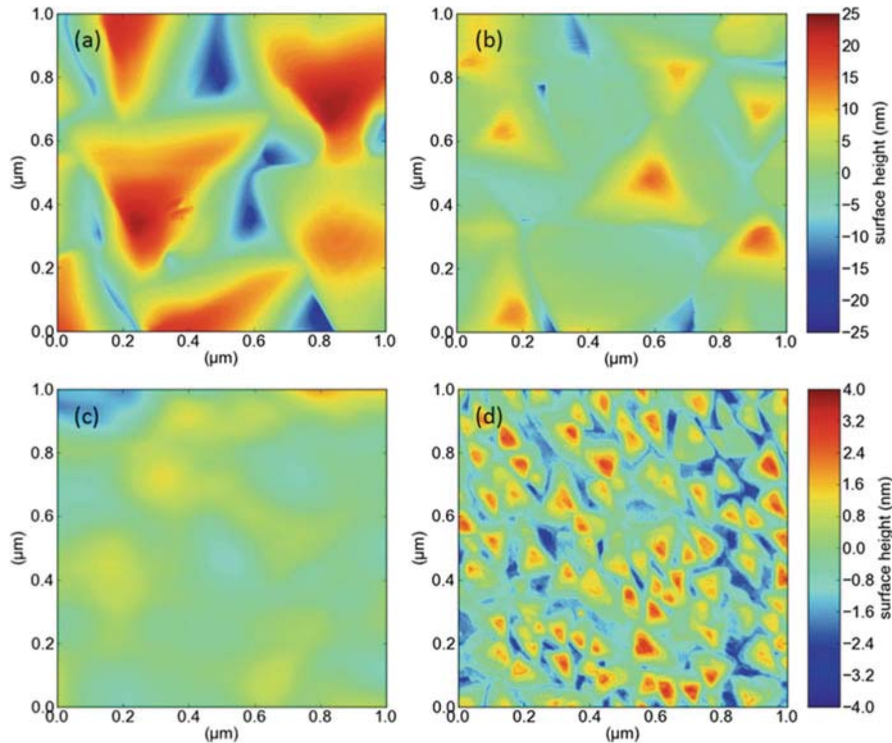

Fig. 11.3 AFM images of Bi_2Te_3 and Bi_2Se_3 films grown with the Te_2/Bi BEP ratio of 10 and Se_2/Bi BEP ratio of 20, respectively. (**a**) 210-nm-thick Bi_2Te_3; (**b**) 215-nm-thick Bi_2Se_3; (**c**) 15-nm-thick Bi_2Te_3; (**d**) 15-nm-thick Bi_2Se_3. After ref. [31]

ratio of 10 for Bi_2Te_3 and Se_2/Bi ratio of 20 for Bi_2Se_3. The thicknesses of the Bi_2Te_3 and Bi_2Se_3 layers shown in Fig. 11.3a, b are 210 and 215 nm, respectively, and the thicknesses of the films corresponding to Fig. 11.3c, d are 15 nm.

The images show many hills of triangular shape (spirals) aligned along specific orientations. Our results agree with other reports on Bi_2Te_3 [22] and Bi_2Se_3 [26] films, suggesting that the growth of TI films takes place by a spiral growth mode, with fast surface diffusion of Bi and Se/Te adatoms to existing Bi_2Se_3 or Bi_2Te_3 island edges due to weak interactions between these adatoms and the substrate [29, 30]. Such growth mode can be seen especially clearly in Fig. 11.3d where many small triangular terraces are observed for a 15-nm-thick Bi_2Se_3 layer, indicating initial 2D island formation for very thin films [27]. This result also suggests that the mobility of Bi adatoms is much slower on the Bi_2Se_3 surface than on Bi_2Te_3, most likely due to different chemical bond strengths of Bi–Te and Bi–Se. Note, however, that as the growth proceeds, the surface morphology of Bi_2Se_3 eventually becomes similar to that of Bi_2Te_3. It is already known in this connection that the surface morphology of TI films is dramatically affected by the group-VI/Bi BEP ratio and by the growth rate [22]. In the case of Bi_2Se_3 growth, as we decreased the Bi flux, the surface of thin Bi_2Se_3 layers became much smoother, becoming Bi_2Te_3-like.

The detailed growth mechanism of TI films is described in [34]: the growth of Bi_2Se_3 and Bi_2Te_3 on epitaxial GaAs (001) begins with 2D nucleation, and the spiral growth follows by pinning of the 2D growth fronts at domain boundaries that are created during the coalescence of the 2D islands. Winding of the growth fronts around these pinning centers leads to triangular shape domains (or spirals) that were already referred to. It should be noted that due to the symmetry mismatch between the hexagonal lattices of TI films and the cubic symmetry of the GaAs (001) surface, along with the weak interaction with the substrate surface, two types of rotation domains could form in the TIs films. This is displayed very clearly by the opposite orientation of the triangle islands in Fig. 11.3b.

11.4 Structure Investigations

The structures of TI samples grown by MBE were characterized by Raman spectroscopy, Raman mapping, transmission electron microscopy (TEM), and high-resolution X-ray diffraction (HR-XRD). Micro Raman spectroscopy was performed with laser excitation at 532-nm (power ~0.8 mW). The results, shown in Fig. 11.4a, b, reveal three of the characteristic peaks for Bi_2Se_3 [at ~71 cm^{-1} (A^1_{1g}), 131 cm^{-1} (E^2_g), and 174 cm^{-1} (A^2_{1g})], and two of the characteristic peaks for Bi_2Te_3 [at ~102 cm^{-1} (E^2_g) and 134 cm^{-1} (A^2_{1g})]. The peaks observed in these two TI materials are consistent with the lattice vibration modes reported earlier [31]. In Fig. 11.4c, d, representative Raman maps (showing Raman shift of the Raman peak E^2_g as a function of position) are plotted for Bi_2Te_3 (Fig. 11.4c) and Bi_2Se_3 (Fig. 11.4d). These Raman maps show that the differences of the Raman shift are less than ~1 cm^{-1} within a scan area of 15×15 μm, indicating impressively a high uniformity of the films.

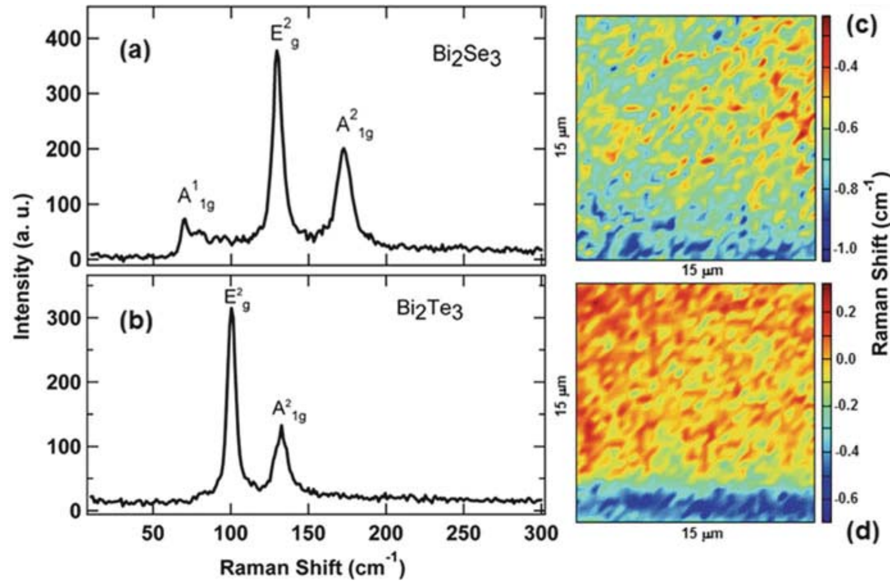

Fig. 11.4 (**a**, **b**) Raman spectra measured on thin Bi_2Se_3 and Bi_2Te_3 films. (**c**, **d**) Maps of Raman shift (relative to bulk) for Bi_2Se_3 and Bi_2Te_3 films, respectively, using the peak E^2_g Raman peak. Adapted from ref. [30, 31]

The microstructure of the films was determined using cross section transmission electron microscopy (XTEM). Samples were prepared for TEM examination using standard mechanical polishing and argon-ion-milling, with the sample held at liquid-nitrogen temperature during the milling process in order to avoid unintentional ion-milling artifacts. In Fig. 11.5, XTEM images of Bi_2Te_3 and Bi_2Se_3 layers grown on GaAs (001) buffers show the lattice structure of both the TI films and the GaAs substrate near their interfaces. Clean interfaces without any amorphous phases are observed, similar to those reported for films grown on GaAs (111) substrates [27]. The highly parallel QLs—Te(Se)-Bi-Te(Se)-Bi-Te(Se)—are visible in both Bi_2Te_3 and Bi_2Se_3 films, marked by the symbol "**I**" in the figure. From Fig. 11.5 it appears that the highly parallel QLs in Bi_2Se_3 film extend over a significantly longer range than those in Bi_2Te_3 films, indicating that a particularly strong internal self-correction process is occurring in Bi_2Se_3 films as the growth proceeds. In addition, despite the symmetry mismatch between the hexagonal lattices of the TI films and the fourfold cubic symmetry of the GaAs (001) surface, the TEM images show that both TI films are highly uniform, and that their crystallinity is comparable to that of films grown on substrates with hexagonal surface structure.

In the case of Bi_2Se_3 films, domain boundaries can often be observed in XTEM images. In Fig. 11.6, the XTEM image of Bi_2Se_3 layer grown on GaAs (100) buffer clearly shows the boundaries between two rotation domains. Two interesting features can be seen in the images: first, the QLs crossing the domain boundaries are

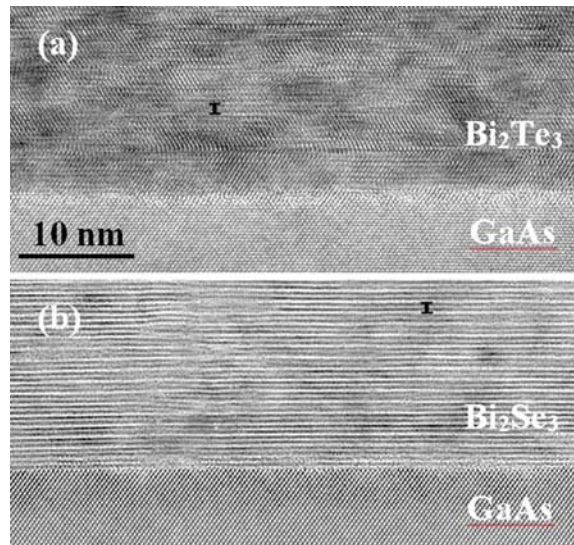

Fig. 11.5 HRTEM images showing cross sections of topological insulator (**a**) Bi_2Te_3 and (**b**) Bi_2Se_3 grown by MBE on a GaAs (001) substrate. The distances between QLs (~1 nm) are marked by "**I**." After ref. [31]

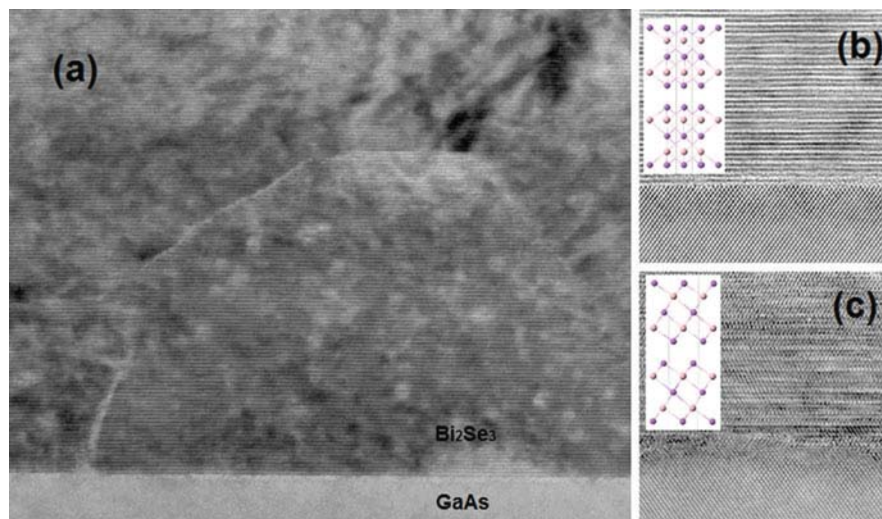

Fig. 11.6 (**a**) TEM images showing cross sections of topological insulator Bi_2Se_3 grown by MBE on a GaAs (001) substrate. (**b**, **c**) HRTEM images showing cross sections of topological insulator Bi_2Se_3 with two different lattice alignments with respect to the GaAs (110) plane

aligned on the same plane, suggesting that this boundary resulted from two types of rotation domains instead of antiphase boundaries or stacking faults; second, one domain is totally enclosed by the other, suggesting that some domains expand faster than other domains. In Fig. 11.6b, c, the high-resolution cross section images clearly

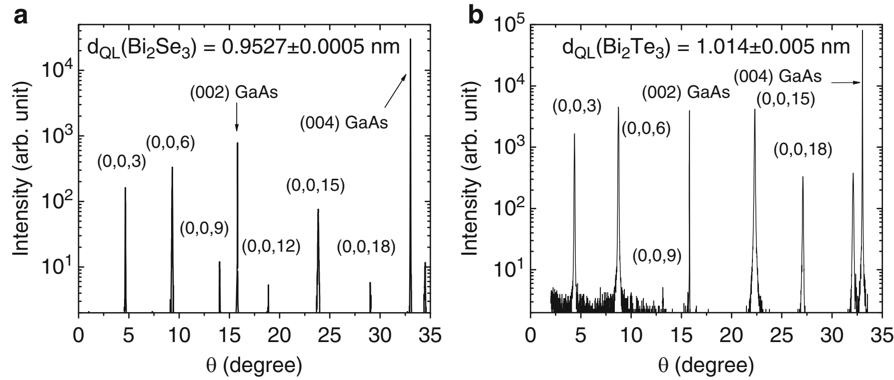

Fig. 11.7 XRD data obtained for (**a**) Bi_2Se_3 and (**b**) Bi_2Te_3 films grown on a GaAs (001) substrate

show two different lattice alignments with respect to the underlying GaAs lattice, as indicated schematically by the lattices shown in the insets. These TEM images thus confirm our observations from RHEED and AFM studies.

The overall crystallinity of the TI films was evaluated by HR-XRD using the Cu $K\alpha_1$ radiation line. Figure 11.7 shows XRD patterns that were obtained from (a) a 233-nm-thick Bi_2Te_3 film and (b) a 180-nm-thick Bi_2Se_3 film. Strong reflections from {003}-type lattice planes of the TI are clearly visible, indicative of the highly directional *c*-axis growth of the film. The full-width-at-half-maximum for the (0,0,6) plane indicates that the crystallinity of Bi_2Se_3 is considerably better than that of Bi_2Te_3 (108 versus 234 s). The QL thicknesses were calculated from the XRD data, giving $d_{QL} = 1.014 \pm 0.005$ nm for Bi_2Te_3 and $d_{QL} = 0.9527 \pm 0.0005$ nm for Bi_2Se_3, respectively (here the uncertainties correspond to 1σ). Both values are consistent with the values of 1.016 nm for bulk Bi_2Te_3 [32] and 0.9545 nm for bulk Bi_2Se_3 [33].

11.5 $Bi_2(TeSe)_3$ Ternary Alloy

In addition to exploration of the binary TI compounds described above, we have also grown a series of ternary Bi-chalcogenide alloys such as $Bi_2(Te_xSe_{1-x})_3$. Such alloys, including their ordered compounds such as $Bi_2Te_2Se_1$, are naturally expected to have a large bulk resistivity owing to several mechanisms [34, 35] that are not present in the binary TIs, thus making them of special interest for those TI studies where the high conductivity of the bulk acts to obscure the topological effects associated with surface states. The specific mechanisms which tend to increase the bulk resistivity of such alloys are primarily the following: (1) the formation of Se vacancies is expected to be suppressed in ternary alloys, because the Se ion trapped

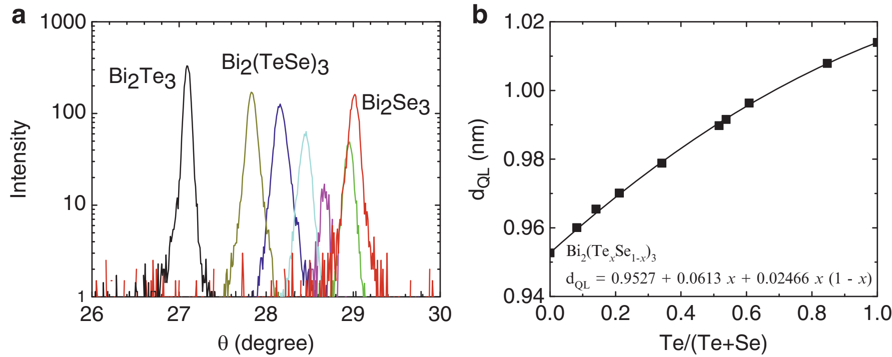

Fig. 11.8 (**a**) XRD spectra measured on a series of $Bi_2(TeSe)_3$ alloy films showing the (0,0,18) reflection peak. (**b**) QL thicknesses d_{QL} calculated from XRD data for a series of $Bi_2(TeSe)_3$ films plotted as a function of Te/(Te + Se) ratio

between two Bi atoms is less exposed to evaporation due to stronger chemical bonding with Bi that occurs in this position; (2) the formation of Te anti-site defects between Te and Se layers is also expected to be suppressed because of preferential bonding between Se and Bi, in contrast to the weak Se–Te bonding; (3) under proper conditions, the formation of ordered Te-Bi-Se-Bi-Te quintuple layers (QLs) can also be achieved in such ternary combinations of Bi, Te, and Se, minimizing the additional disorder that could be caused by Se/Te randomness, consecutively reducing the bulk carrier concentration.

With this in mind, we have also carried out the growth of a series of $Bi_2(TeSe)_3$ alloy films on GaAs (001) substrates using various $Te_2/(Te_2 + Se_2)$ BEP ratios. The ternary films were grown in a Te-rich regime by varying Se_2 flux, with a constant of Te_2/Bi BEP of around 10. As in the case of the binary TI films discussed above, the XRD spectra taken on the ternary $Bi_2(TeSe)_3$ alloy films reveal only reflections from the {003}-type lattice planes, again indicating highly directed *c*-axis growth of these films. X-ray rocking curves yielded a full-width-at-half maximum of 0.2–0.5°. Figure 11.8a shows the (0,0,18) reflection peaks of the XRD spectra obtained for a series of $Bi_2(TeSe)_3$ films, indicating that a wide spectrum of mixed $Bi_2(TeSe)_3$ alloys can be obtained, thus also representing a step toward realizing structures with ordered Te-Bi-Se-Bi-Te QLs. The QL thicknesses d_{QL} were calculated from the XRD data. As shown in Fig. 11.8b, the quintuple layer thickness d_{QL} is not fully linear with the Te/(Te + Se) ratio of the $Bi_2(TeSe)_3$ alloy composition, which was measured by Rutherford backscattering spectrometry. Such nonlinearity (bowing) suggests that the chemical stoichiometric ratios [i.e., Te/(Te + Se)] might be different between the center Te/Se plane and the top/bottom Te/Se planes of QL structure. We attribute this interesting nonlinearity to the fact that Bi favors bonding with Se rather than with Te. This result agrees with our AFM measurements.

11.6 ARPES and Transport

The ARPES measurements were performed at beamline 10.0.1 (HERS) of the Advanced Light Source, Berkeley, CA, equipped with a VG-Scienta R4000 electron analyzer. The 330-nm-thick film sample was cleaved in situ for full exposure of a pristine surface, and was measured at ~20 K in a vacuum better than 5×10^{-11} Torr.

Figure 11.9 shows ARPES data of a 330-nm-thick $Bi_{1.95}Te_{0.25}Se_{2.8}$ film, where the chemical stoichiometry of this alloy was measured by Rutherford backscattering spectrometry. Figure 11.9a presents typical ARPES constant energy maps at three different binding energies. The ARPES Fermi map (left panel of Fig. 11.9a) shows clearly the remnant photoemission intensity from the bulk conduction band (BCB) around Γ, and the topological surface state (Dirac cone) circumventing it. No sign

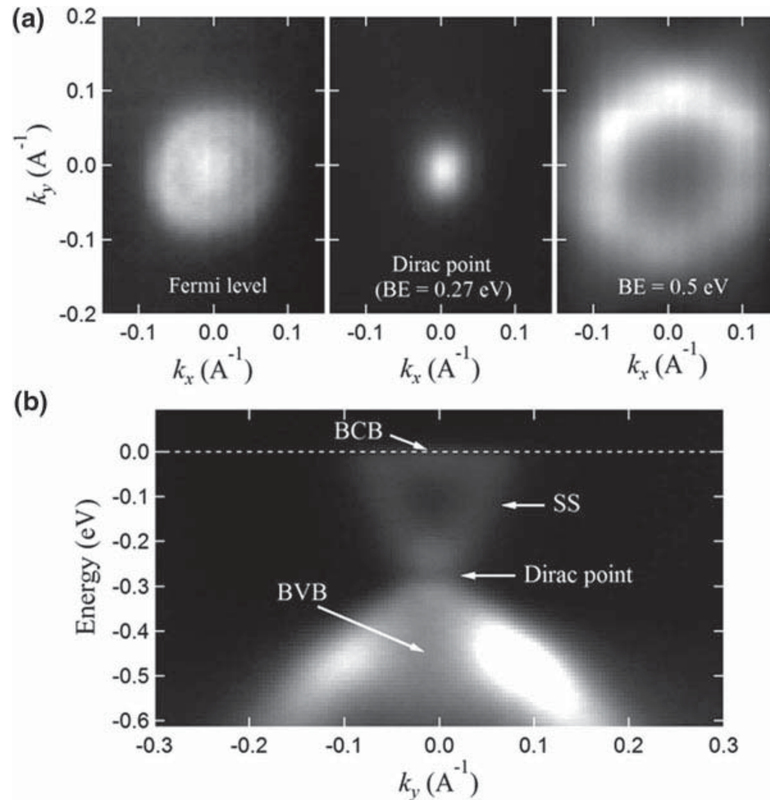

Fig. 11.9 ARPES data obtained on a 330-nm-thick $Bi_{1.95}Te_{0.25}Se_{2.8}$ film. (**a**) Constant energy maps at three selected binding energies (BEs). It is clear from the figure that the Dirac point is fully exposed for this film. (**b**) ARPES *k-E* map along the *Γ-M* direction (k_y). *BCB* bulk conduction band, *BVB* bulk valence band, *SS* surface state (*Dirac cone*)

of hexagonal warping is seen at the Dirac cone, since the Fermi level of this film is located at only 0.27 eV above the Dirac point, where the influence of the sixfold symmetry of the bulk bands on the surface state is weak. From the map taken at 0.27 eV binding energy (middle panel of Fig. 11.9b), it is seen that the Dirac point is fully exposed. The top of the bulk valence band (BVB) lies lower than the Dirac point. At higher binding energies, the influence of the bulk symmetry becomes more visible (right panel of Fig. 11.9a), as the band contour changes to a hexagonal shape. Figure 11.9b presents an ARPES k–E map taken along the Γ-M momentum space direction, where the BVB, BCB, and SS (surface state) are clearly marked. The presence of BCB below the Fermi level confirms the bulk conducting nature of the film. One noteworthy observation from this map is that the photoemission intensity experiences a slight suppression at the Dirac point, forming a gap-like feature. Several reasons might lead to this phenomenon. (1) The remaining film after the in situ cleaving may be so thin that the top and bottom layers of the film interact with each other, giving rise to a tunneling gap resolved by other studies. (2) Strong spatial fluctuations caused by surface impurities may prevent the momentum from being a good quantum number, which in turn gives rise to a gap-like feature in spatially averaged measurements such as ARPES [36].

We have carried out low-temperature (T) magnetotransport measurements on both Bi_2Se_3 and Bi_2Te_3 films. Our magnetotransport data show pronounced cusp-like behavior in both films, consistent with weak anti-localization (WAL) [37, 38]. As an example, we have performed low-T transport measurements on a Bi_2Se_3 film (6 nm). The magnetotransport data exhibit resistance suppression near zero B-field (Fig. 11.10c), consistent with WAL related to spin-momentum locking and spin-orbit coupling [9, 39, 40]. WAL has been recently extensively used in TI study to probe the coherent transport properties of both the bulk and the surface carriers, e.g., coherence channel number and length [42, 44].

In this work, all our Hall-bar devices are patterned into a 15-μm-width by standard lithography, with Cr/Au ohmic contacts deposited by an e-beam evaporator. To study electric field-modulated transport, the Bi_2Se_3 Hall-bars are capped by a 35-nm Al_2O_3 dielectric layer using atomic layer deposition. Figure 11.10a shows one of our typical top-gated Hall-bar field effect transistor (FET) devices with Al_2O_3 dielectric. The transport measurements are performed in cryostats using standard low-frequency lock-in techniques.

As shown in Fig. 11.10b, our 6-nm Bi_2Se_3 film exhibits a transition from a high-T metallic behavior to a low-T insulating behavior, indicating that the bulk conduction starts to be reduced at low-T. At the base T (1.5 K), the electron concentration (n_e) and mobility (μ) for this specific Bi_2Se_3 film extracted from the Hall data (Fig. 11.10c) are $n_e = 1.5–3.5 \times 10^{13}$ cm^{-2} ($2.5–5.9 \times 10^{19}$ cm^{-3}) and μ ~140 cm^2/V s, respectively, indicating that there still remains a significant amount of bulk carriers. Moreover, near the zero B-field region, R_{xx} data shows a downward cusp-like behavior (WAL feature). Figure 11.10d shows the effects of the electric field on the sheet resistance (R_{xx}) at the base $T = 1.5$ K. In this sample with a substantial bulk carrier density, R_{xx} is only weakly modulated by the gate voltage (V_g). The observed WAL can be fit well by a two-component Hikami–Larkin–Nagaoka (HLN) equation in the strong

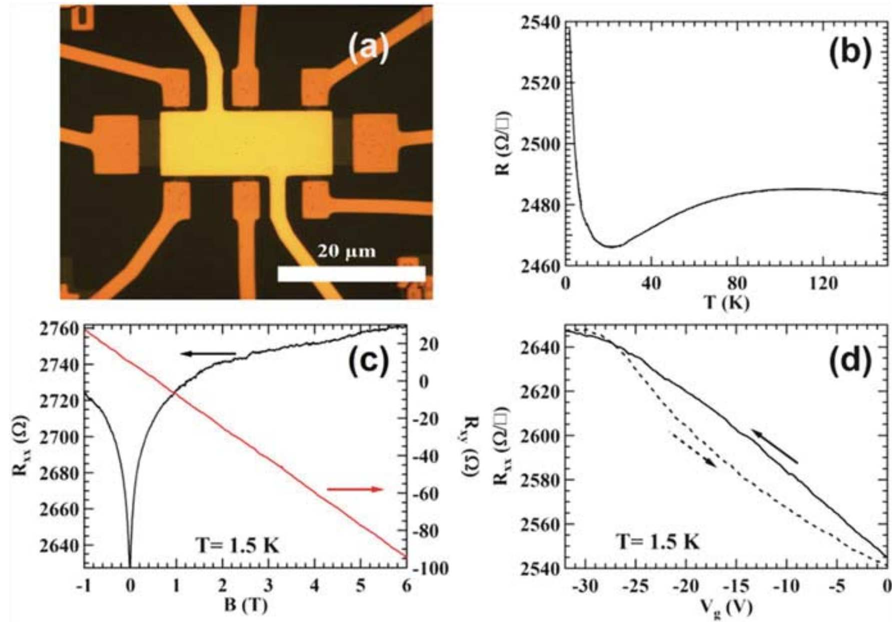

Fig. 11.10 (**a**) Optical image of a typical top-gated Bi_2Se_3 Hall-bar device with high-*k* dielectric (Al_2O_3). (**b**) Temperature dependence of the resistance for a typical 6 nm Bi_2Se_3 film. (**c**) Magnetoresistance (R_{xx} and R_{xy}) for the 6-nm Bi_2Se_3 device at $T = 1.5$ K, showing a typical WAL behavior in the low *B*-field region. (**d**) Electric field (V_g) modulated sheet resistance at $T = 1.5$ K

spin-orbit coupling limit [41]. The HLN analysis gives two important coherent transport parameters, phase coherence length ($\boldsymbol{l}_c$) and coherence channel number ($\boldsymbol{A}$), where $\boldsymbol{A} = -1$ corresponds to one single coherence channel. Our results for this sample show $\boldsymbol{A} = -1.2$ and $\boldsymbol{l}_c = 42.6$ nm, both parameters being only weakly depending on V_g.

11.7 Concluding Remarks

In this exploratory study, we have successfully grown high quality epitaxial films of Bi_2Te_3, Bi_2Se_3, and their alloys on GaAs (001) substrates even though there is a mismatch between the hexagonal lattices of Bi_2Te_3 and Bi_2Se_3 TI films and the fourfold cubic symmetry of the GaAs (001) surface. The films are highly uniform, and their crystalline quality is comparable to that of films grown on substrates with hexagonal or threefold symmetric surfaces. Examination of the TI film surfaces by AFM reveals a spiral growth mode, the same as reported previously for TI films. Measurements of ARPES were also carried out, and confirmed the TI properties. Magnetotransport studies performed on these Bi_2Te_3 and Bi_2Se_3 films clearly show

signatures of 2D transport, including effects of WAL. Future studies of TI films grown on GaAs (001) substrates should contribute toward a better understanding of the process of formation of TI-layered structures in MBE growth. Fabrication of TI films on substrates compatible with commonly used orientations also opens important options for future spin-based devices. Opportunities such as the realization of spin-momentum locking in the surface bands of interest for spintronic applications [42, 43, 45] and the realization of quantized magneto-electric effects [44, 45] suggest themselves in this context. As a more distant but highly exciting prospect, such studies would also lay the ground for further work for advancing magnetic-monopole-like image charges [46], as well as for obtaining structures that can host Majorana fermions at topological insulator/superconductor interfaces, that hold promise for applications in fault-tolerant topological quantum computing [47, 48].

Acknowledgements This work was supported by NSF Grant DMR10-05851 (ND); NSF grant ECCS10-02114 and an AFOSR Grant FA9550-10-1-0129 (ASU); and DARPA MESO program (Purdue). The authors acknowledge use of facilities in the John M. Cowley Center for High Resolution Electron Microscopy at Arizona State University. The authors also thank Dr. K.M. Yu at Lawrence Berkeley National Laboratory for providing the chemical stoichiometric ratios of $Bi_2(TeSe)_3$ alloys using Rutherford backscattering spectrometry.

References

1. Kane, C.L., Mele, E.J.: Quantum spin Hall effect in graphene. Phys. Rev. Lett. **95**, 226801 (2005)
2. Kane, C.L., Mele, E.J.: Z_2 topological order and the quantum spin Hall effect. Phys. Rev. Lett. **95**, 146802 (2005)
3. Bernevig, B.A., Hughes, T.L., Zhang, S.-C.: Quantum spin Hall effect and topological phase transition in HgTe quantum wells. Science **314**, 1757 (2006)
4. König, M., Wiedmann, S., Brüne, C., Roth, A., Buhmann, H., Molenkamp, L.W., Qi, X.-L., Zhang, S.-C.: Quantum spin Hall insulator state in HgTe quantum wells. Science **318**, 766 (2007)
5. Qi, X.-L., Zhang, S.-C.: The quantum spin Hall effect and topological insulators. Phys. Today **63**, 33 (2010)
6. Fu, L., Kane, C.L., Mele, E.J.: Topological insulators in three dimensions. Phys. Rev. Lett. **98**, 106803 (2007)
7. Moore, J.E., Balents, L.: Topological invariants of time-reversal-invariant band structures. Phys. Rev. B **75**, 121306 (2007)
8. Hasan, M.Z., Kane, C.L.: *Colloquium*: Topological insulators. Rev. Mod. Phys. **82**, 3045 (2010)
9. Bychkov, Y.A., Rashba, E.I.: Properties of a 2D electron gas with lifted spectral degeneracy. JETP Lett. **39**, 66 (1984)
10. Liu, C.-X., Qi, X.-L., Zhang, H., Dai, X., Fang, Z., Zhang, S.-C.: Model hamiltonian for topological insulators. Phys. Rev. B **82**, 045122 (2010)
11. Shan, W.-Y., Lu, H.-Z., Shen, S.-Q.: Effective continuous model for surface states and thin films of three-dimensional topological insulators. New J. Phys. **12**, 043048 (2010)
12. Hsieh, D., Qian, D., Wray, L., Xia, Y., Hor, Y.S., Cava, R.J., Hasan, M.Z.: A topological dirac insulator in a quantum spin Hall phase. Nature **452**, 970 (2008)

13. Xia, Y., Qian, D., Hsieh, D., Wray, L., Pal, A., Lin, H., Bansil, A., Grauer, D., Hor, Y.S., Cava, R.J., Hasan, M.Z.: Observation of a large-gap topological-insulator class with a single Dirac cone on the surface. Nat. Phys. **5**, 398 (2009)
14. Zhang, G., Qin, H., Teng, J., Guo, J., Guo, Q., Dai, X., Fang, Z., Wu, K.: Quintuple-layer epitaxy of thin films of topological insulator Bi_2Se_3. Appl. Phys. Lett. **95**, 053114 (2009)
15. Chen, Y.L., Analytis, J.G., Chu, J.H., Liu, Z.K., Mo, S.K., Qi, X.L., Zhang, H.J., Lu, D.H., Dai, X., Fang, Z., Zhang, S.-C., Fisher, I.R., Hussain, Z., Shen, Z.-X.: Experimental realization of a three-dimensional topological insulator, Bi_2Te_3. Science **325**, 178 (2009)
16. Hsieh, D., Xia, Y., Qian, D., Wray, L., Dil, J.H., Meier, F., Osterwalder, J., Patthey, L., Fedorov, A.V., Lin, H., Bansil, A., Grauer, D., Hor, Y.S., Cava, R.J., Hasan, M.Z.: Observation of time-reversal-protected single-dirac-cone topological-insulator states in Bi_2Te_3 and Sb_2Te_3. Phys. Rev. Lett. **103**, 146401 (2009)
17. Hsieh, D., Xia, Y., Wray, L., Qian, D., Pal, A., Dil, J.H., Osterwalder, J., Meier, F., Bihlmayer, G., Kane, C.L., Hor, Y.S., Cava, R.J., Hasan, M.Z.: Observation of unconventional quantum spin textures in topological insulators. Science **323**, 919 (2009)
18. Roushan, P., Seo, J., Parker, C.V., Hor, Y.S., Hsieh, D., Qian, D., Richardella, A., Hasan, M.Z., Cava, R.J., Yazdani, A.: Topological surface states protected from backscattering by chiral spin texture. Nature **460**, 1106 (2009)
19. Chen, X., Ma, X.-C., He, K., Jia, J.-F., Xue, Q.-K.: Molecular Beam Epitaxial Growth of Topological Insulators. Adv. Mater. **23**, 1162 (2011)
20. Li, H.D., Wang, Z.Y., Guo, X., Wong, T.L., Wang, N., Xie, M.H.: Growth of multilayers of Bi_2Se_3/ZnSe: Heteroepitaxial interface formation and strain. Appl. Phys. Lett. **98**, 043104 (2011)
21. Liu, M., Chang, C.-Z., Zhang, Z., Zhang, Y., Ruan, W., He, K., Wang, L.L., Chen, X., Jia, J.-F., Zhang, S.-C., Xue, Q.-K., Ma, X., Wang, Y.: Electron interaction-driven insulating ground state in Bi_2Se_3 topological insulators in the two-dimensional limit. Phys. Rev. B **83**, 165440 (2011)
22. Zhang, G.H., Qin, H.J., Chen, J., He, X.Y., Lu, L., Li, Y.Q., Wu, K.H.: Growth of topological insulator Bi_2Se_3 thin films on $SrTiO_3$ with large tunability in chemical potential. Adv. Funct. Mater. **21**, 2351 (2011)
23. Richardella, A., Zhang, D.M., Lee, J.S., Koser, A., Rench, D.W., Yeats, A.L., Buckley, B.B., Awschalom, D.D., Samarth, N.: Coherent heteroepitaxy of Bi_2Se_3 on GaAs (111)B. Appl. Phys. Lett. **97**, 262104 (2010)
24. Sadowski, J., Mathieu, R., Svedlindh, P., Domagała, J.Z., Bak-Misiuk, J., Światek, K., Karlsteen, M., Kanski, J., Ilver, L., Åsklund, H., Södervall, U.: Structural and magnetic properties of GaMnAs layers with high Mn-content grown by migration-enhanced epitaxy on GaAs(100) substrates. Appl. Phys. Lett. **78**, 3271 (2001)
25. Krebs, J.J., Jonker, B.T., Prinz, G.A.: Properties of Fe single-crystal films grown on (100) GaAs by molecular-beam epitaxy. J. Appl. Phys. **61**, 2596 (1987)
26. Liu, X., Smith, D.J., Fan, J., Zhang, Y.-H., Cao, H., Chen, Y.P., Leiner, J., Kirby, B.J., Dobrowolska, M., Furdyna, J.K.: Structural properties of Bi_2Te_3 and Bi_2Se_3 topological insulators grown by molecular beam epitaxy on GaAs(001) substrates. Appl. Phys. Lett. **99**, 171903 (2011)
27. Liu, X., Smith, D.J., Cao, H., Chen, Y.P., Fan, J., Zhang, Y.-H., Pimpinella, R.E., Dobrowolska, M., Furdyna, J.K.: Characterization of Bi_2Te_3 and Bi_2Se_3 topological insulators grown by MBE on (001) GaAs substrates. J. Vac. Sci. Technol. B **30**, 02B103 (2012)
28. Shufflebotham, P.K., Card, H.C., Kao, K.C., Thanailakis, A.: Amorphous silicon–tellurium alloys. J. Appl. Phys. **60**, 2036 (1986)
29. Li, H.D., Wang, Z.Y., Kan, X., Guo, X., He, H.T., Wang, Z., Wang, J.N., Wong, T.L., Wang, N., Xie, M.H.: The van der Waals epitaxy of Bi_2Se_3 on the vicinal Si(111) surface: an approach for preparing high-quality thin films of a topological insulator. New J. Phys. **12**, 103038 (2010)
30. Liu, Y., Weinert, M., Li, L.: Spiral growth without dislocations: Molecular beam epitaxy of the topological insulator Bi_2Se_3 on epitaxial Graphene/SiC(0001). Phys. Rev. Lett. **108**, 115501 (2012)

31. Richter, W., Kohler, H., Becker, C.R.: A Raman and far-infrared investigation of phonons in the rhombohedral V_2–VI_3 compounds Bi_2Te_3, Bi_2Se_3, Sb_2Te_3 and $Bi_2(Te_{1-x}Se_x)_3$ $(0 < x < 1)$, $(Bi_{1-y}Sb_y)_2Te_3$ $(0 < y < 1)$. Phys. Status Solidi B **84**, 619 (1977)
32. Jenkins, J.O., Rayne, J.A., Ure, J.R.W.: Elastic moduli and phonon properties of Bi_2Te_3. Phys. Rev. B **5**, 3171 (1972)
33. Nakajima, S.: The crystal structure of $Bi_2Te_{3-x}Se_x$. J. Phys. Chem. Solids **24**, 479 (1963)
34. Ren, Z., Taskin, A.A., Sasaki, S., Segawa, K., Ando, Y.: Large bulk resistivity and surface quantum oscillations in the topological insulator Bi_2Te_2Se. Phys. Rev. B **82**, 241306(R) (2010)
35. Sokolov, O.B., Skipidarov, S.Y., Duvankov, N.I., Shabunina, G.G.: Chemical reactions on the Bi_2Te_3–Bi_2Se_3 section in the process of crystal growth. J. Cryst. Growth **262**, 442 (2004)
36. Xu, S.-Y., Wray, L. A., Alidoust, N., Xia, Y., Neupane, M., Liu, C., Ji, H.-W., Jia, S., Cava, R. J., Hasan, M. Z.: Dirac point spectral weight suppression and surface “gaps” in nonmagnetic and magnetic topological insulators. arXiv:1206.0278 (2012)
37. He, H.T., Wang, G., Zhang, T., Sou, I.K., Wong, G.K.L., Wang, J.N., Lu, H.Z., Shen, S.Q., Zhang, F.C.: Impurity effect on weak antilocalization in the topological insulator Bi_2Te_3. Phys. Rev. Lett. **106**, 166805 (2011)
38. Steinberg, H., Laloe, J.-B., Fatemi, V., Moodera, J.S., Jarillo-Herrero, P.: Electrically tunable surface-to-bulk coherent coupling in topological insulator thin films. Phys. Rev. B **84**, 233101 (2011)
39. Moore, J.E.: The birth of topological insulators. Nature **464**, 194 (2010)
40. Qi, X.-L., Zhang, S.-C.: Topological insulators and superconductors. Rev. Mod. Phys. **83**, 1057 (2011)
41. Hikami, S., Larkin, A.I., Nagaoka, Y.: Spin-orbit interaction and magnetoresistance in the two dimensional random system. Prog. Theor. Phys. **63**, 707 (1980)
42. Ohno, H.: A window on the future of spintronics. Nat. Mater. **9**, 952 (2010)
43. Vobornik, I., Manju, U., Fujii, J., Borgatti, F., Torelli, P., Krizmancic, D., Hor, Y.S., Cava, R.J., Panaccione, G.: Magnetic proximity effect as a pathway to spintronic applications of topological insulators. Nano Lett. **11**, 4079 (2011)
44. Tse, W.-K., MacDonald, A.H.: Magneto-optical and magnetoelectric effects of topological insulators in quantizing magnetic fields. Phys. Rev. B **82**, 161104 (2010)
45. Essin, A.M., Moore, J.E., Vanderbilt, D.: Magnetoelectric polarizability and axion electrodynamics in crystalline insulators. Phys. Rev. Lett. **102**, 146805 (2009)
46. Qi, X.L., Li, R., Zang, J., Zhang, S.C.: Inducing a magnetic monopole with topological surface states. Science **323**, 1184 (2009)
47. Fu, L., Kane, C.: Superconducting proximity effect and majorana fermions at the surface of a topological insulator. Phys. Rev. Lett. **100**, 096407 (2008)
48. Nayak, C., Simon, S.H., Stern, A., Freedman, M., Das Sarma, S.: Non-Abelian anyons and topological quantum computation. Rev. Mod. Phys. **80**, 1083 (2008)